npj computational materials

www.nature.com/npjcompumats

ARTICLE OPEN

Microscopic theory of light-induced ultrafast skyrmion excitation in transition metal films

Emil Viñas Boström[1]✉, Angel Rubio[1,2]✉ and Claudio Verdozzi[3]✉

Magnetic skyrmions are topological excitations of great promise for compact and efficient memory storage. However, to interface skyrmionics with electronic devices requires efficient and reliable ways of creating and destroying such excitations. In this work, we unravel the microscopic mechanism behind ultrafast skyrmion generation by femtosecond laser pulses in transition metal thin films. We employ a theoretical approach based on a two-band electronic model, and show that by exciting the itinerant electronic subsystem with a femtosecond laser ultrafast skyrmion nucleation can occur on a 100 fs timescale. By combining numerical simulations with an analytical treatment of the strong *s*–*d* exchange limit, we identify the coupling between electronic currents and the localized *d*-orbital spins, mediated via Rashba spin–orbit interactions among the itinerant electrons, as the microscopic and central mechanism leading to ultrafast skyrmion generation. Our results show that an explicit treatment of itinerant electron dynamics is crucial to understand optical skyrmion generation.

npj Computational Materials (2022)8:62 ; https://doi.org/10.1038/s41524-022-00735-5

INTRODUCTION

Topological magnetic excitations are of large interest both from a fundamental point of view and for the construction of compact and energy-efficient memory and computational devices[1–10]. A notable example is magnetic skyrmions, chiral topological spin configurations stabilized through competition of exchange, Dzyaloshinskii–Moriya (DM), and Zeeman or anisotropy interactions. Skyrmions have generated much attention due to their potential for realizing race track memories[11–13] and quantum computation devices[5,14,15]. However, to exploit magnetic topological excitations for technological purposes requires efficient ways of writing, deleting, and manipulating them on short time scales and with high spatial precision. As demonstrated in recent experiments[16–18], a promising method to create small skyrmion clusters is by irradiating chiral magnetic films with femtosecond light pulses. While several works have addressed the process of laser-induced skyrmion excitation[19–22], an adequate understanding of the underlying microscopic mechanism is still lacking.

More generally, recent developments in material engineering via light–matter interactions and interlayer stacking/twisting[23–29] raise the question of how light can be used to tailor chiral, non-trivial magnetic textures. While previous work has been mostly confined to isolated spin or electron systems[17–22,30–32], thus neglecting the dynamical interplay of itinerant electrons and localized magnetic moments, this interplay is both ubiquitous in real materials and has a significant influence on the dynamics of magnetic systems[30–36]. In particular, we here demonstrate that *the coupling of itinerant electrons and localized spins is a key factor in understanding the optical generation of chiral topological spin textures*. Hence, to fully exploit material engineering for optomagnetic phenomena and applications, an explicit description of the role of the itinerant electrons is necessary.

To substantiate our statement, we here propose a framework to address the dynamical interaction of itinerant electrons and localized spins out of equilibrium and to study how light can be used to excite chiral topological spin textures. This is exemplified by the skyrmion creation process, where we identify a microscopic mechanism for ultrafast skyrmion nucleation via laser excitation of the itinerant electrons. Specifically, we consider a two-band model of coupled itinerant *s*-electrons and strongly correlated *d*-electrons in two dimensions, where the *d*-electrons are described by an effective spin Hamiltonian. We find that (i) when the *s*–*d* exchange is the largest energy scale in the system, skyrmions are excited on a 100 fs timescale. (ii) The equilibrium phase diagram shows competing spin spiral, ferromagnetic (FM), and skyrmion crystal regions, with a small energy barrier to excite skyrmions from the FM state. Crucially, the energy barrier is tunable via the $s-d$ exchange. (iii) The coupling between the *s*- and *d*-electrons mediated via spin-orbit interactions in the *s*-electron system is essential to describe skyrmion photo-excitation. Our model provides a proof-of-principle of skyrmion photo-excitation via a straightforward protocol and standard laser sources.

RESULTS

Theoretical model

We consider a coupled system of *s*- and *d*-electrons on a square lattice and subject to a laser drive. The light–matter coupling is included via Peierls substitution, where the Peierls phases are $\theta_{ij}(t) = -(e/\hbar)\int_{\mathbf{r}_i}^{\mathbf{r}_i} d\mathbf{r}\cdot\mathbf{A}(\mathbf{r},t)$ and $\mathbf{A}(\mathbf{r},t)$ is the vector potential. For a strongly correlated *d*-band at half-filling, empty and doubly occupied states can be projected out by a time-dependent Schrieffer-Wolff transformation[37,38] (see Supplementary Note 1).

[1]Max Planck Institute for the Structure and Dynamics of Matter, Luruper Chaussee 149, 22761 Hamburg, Germany. [2]Center for Computational Quantum Physics (CCQ), The Flatiron Institute, 162 Fifth Avenue, New York, NY 10010, USA. [3]Division of Mathematical Physics and ETSF, Lund University, PO Box 118, 221 00 Lund, Sweden.
✉email: emil.bostrom@mpsd.mpg.de; angel.rubio@mpsd.mpg.de; claudio.verdozzi@teorfys.lu.se

This results in the Hamiltonian $H(t) = H_s(t) + H_{s-d} + H_d$ with

$$H_s(t) = \sum_{\langle ij \rangle} e^{i\theta_{ij}(t)} c^\dagger_{i\sigma}(-t_s \mathbf{1} + \boldsymbol{\alpha}_{s,ij} \cdot \boldsymbol{\tau})_{\sigma\sigma'} c_{j\sigma'} + \sum_{i\sigma} \epsilon_{si\sigma}(t) \hat{n}_{i\sigma} - \mathbf{B} \cdot \sum_i \hat{\mathbf{s}}_i$$
$$H_{s-d} = -g \sum_i \hat{\mathbf{s}}_i \cdot \hat{\mathbf{S}}_i$$
$$H_d = \sum_{\langle ij \rangle} \left[J_{ij} \hat{\mathbf{S}}_i \cdot \hat{\mathbf{S}}_j + \mathbf{D}_{ij} \cdot (\hat{\mathbf{S}}_i \times \hat{\mathbf{S}}_j) \right] - \mathbf{B} \cdot \sum_i \hat{\mathbf{S}}_i. \quad (1)$$

Here, $c^\dagger_{i\sigma}$ creates an itinerant s-electron at site i with spin projection σ, $\hat{n}_{i\sigma}$ is the s-electron spin density operator at site i, and $\hat{\mathbf{s}}_i = c^\dagger_{i\sigma} \boldsymbol{\tau}_{\sigma\sigma'} c_{i\sigma'}$ and $\hat{\mathbf{S}}_i$ are the s- and d-electron spin operators where $\boldsymbol{\tau}$ denotes the vector of Pauli matrices. Here and in the following, repeated spin indexes are summed over. The hopping amplitude between nearest-neighbor sites i and j is given by t_s, $\boldsymbol{\alpha}_{s,ij}$ accounts for Rashba spin-orbit interactions, and $\epsilon_{si\sigma}$ is the s-electron local potential. $\mathbf{B}$ is an external magnetic field, g the effective s–d exchange, and J_{ij} and $\mathbf{D}_{ij}$ give the exchange and DM interactions (DMIs)[39,40], respectively.

Although the effective spin parameters J_{ij} and $\mathbf{D}_{ij}$ should in principle be time-dependent, a Floquet analysis shows that they deviate significantly from their equilibrium values only for very large electric fields or when $n\hbar\omega \approx U$ (where n is an integer and U is the d-orbital Hubbard interaction)[30–32,34]. Therefore, in what follows, we assume that the dynamic renormalization of the spin parameters is small. This is no serious restriction since this regime can be realized in experiments by tuning the frequency and field strength of the laser. There is in principle also a contribution to the Peierls phases coming from the external magnetic field $\mathbf{B}$, which would lead to an enlarged magnetic unit cell and Landau level formation among the s-electrons. However, for the magnetic fields considered here the ratio Φ/Φ_0 of the magnetic flux to the flux quantum $\Phi_0 = e/2h$ is very small throughout the system (of the order of 10^{-3}), and can thus be neglected. In the effective spin Hamiltonian describing the d-electrons, there is no effect, since any static contribution to the Peierls phases cancels out (see Supplementary Note 1).

We note that in magnetic thin films, skyrmions are often stabilized by an easy-axis anisotropy not included in the spin Hamiltonian. However, since the main effect of the anisotropy is to break the rotational symmetry of the spin system, and to lower the energy of the skyrmion state relative to the spiral state preferred by the DMI, the same role is played by the Zeeman interaction. Neglecting such anisotropies will thus have no qualitative effect on the results below.

In the following, we take the semi-classical limit $\hat{\mathbf{S}}_i \to \langle \hat{\mathbf{S}}_i \rangle \equiv \mathbf{S}_i$, which is exact for $S \to \infty$ and in practice works well for systems with large spins[41–43]. Within the semi-classical approximation, the present model corresponds to a two-dimensional generalization of the model introduced in ref. [33]. To obtain the intertwined dynamics of the d-electron spins and itinerant s-electrons, we solve their coupled equations of motion as described in the "Methods" section.

Relation to previous work

As mentioned in the introduction, previous work on skyrmion photo-excitation has been restricted to isolated spin systems. One proposed explanation relies on local laser-induced heating as described via a stochastic Landau-Lifshitz equation[44]. This leads to thermal skyrmion excitation within 0.1–1 ns[18–20] but misses the microscopic features underlying spin-lattice heating. A second proposal invokes the inverse Faraday effect (IFE), where the laser electric field couples to the system's magnetization via the asymmetric imaginary part of the dielectric tensor[17,21]. However, the IFE is inefficient for atomically thin magnetic films because of the short propagation length and small associated Faraday rotation (see Supplementary Note 3). A third suggestion is to consider electromagnetic vortex beams carrying orbital angular momentum and a net magnetic field[22]. However, this mechanism does not explain skyrmion excitation by linearly and circularly polarized laser pulses, as typically employed in experiments.

Our framework naturally incorporates heating effects via energy transfer between the s- and d-electron systems, and both the IFE and inverse Cotton–Mouton effect (ICME) can be taken into account by additional light–matter coupling terms. Even though the IFE and ICME are negligible in the present context, we show below that laser-induced currents in the s-electron system couple to the d-electron spins via strong s–d exchange and lead to skyrmion excitation on ultrashort timescales.

Creating a skyrmion with light

The dynamics of the system is initiated by a laser pulse with the electric field

$$\mathbf{E}(\mathbf{r}, t) = E e^{-r^2/2\sigma^2} \sin^2\left(\frac{\pi t}{2\tau}\right) \sin(\omega t) \hat{\mathbf{x}} \quad (2)$$

for $t \in (0, 2\tau)$ and zero otherwise. The pulse width is set to $\tau =$ 60 fs, giving a full width at half maximum of 30 fs, and the photon energy is $\hbar\omega = 0.5$ eV. The distance r is measured from the system center, and the spot size of the laser is controlled by the parameter $\sigma = 6a$ where a is the lattice spacing. Taking $a = 5$ Å and field strength of $E = 10^9\,\mathrm{V\,m^{-1}}$, the pulse has an integrated fluence $F = 2.9\,\mathrm{mJ\,cm^{-2}}$ similar to typical experiments[18].

For the spin parameters we take $J = 50$, $D = 25$, and $B = 10$ meV, consistent with the values for the transition metal film CoFeB/Ta[45–47] at a lattice parameter $a = 5$ Å. We include a small Gilbert damping $\alpha_G = 0.01$ in the Landau–Lifshitz equation to mimic a dissipative environment and to stabilize the dynamics at long times. The parameters for the s-electrons are chosen as $t_s = 1$ eV, $\alpha_s = 0.5$ eV, and $\epsilon_{si\sigma} = -B\mathrm{sgn}\,\sigma$. Finally, since typically the direct FM exchange is larger than the s–d hybridization induced antiferromagnetic exchange[48,49], we take $g > 0$.

In Fig. 1, we show the photo-induced nucleation of a Néel skyrmion in a system with 30×30 sites (for Rashba spin–orbit interaction the induced DMI favors Néel skyrmions), starting from an FM state. The skyrmion nucleates by a single spin-flip process, and then expands to a size determined by the magnetic parameters (see Supplementary Note 4). During the subsequent time evolution, the skyrmion remains stable but its radius oscillates. This could indicate that the skyrmion is created in a breathing mode[50,51], however, a full characterization of this excited state is beyond the scope of the present work. The topology of the spin texture is quantified via the lattice topological charge $Q = \sum_i Q_i$ (see "Methods"), where $Q_i = \mp 1$ for a single skyrmion (anti-skyrmion). As seen in Fig. 1b, laser irradiation leads to the excitation of a single skyrmion after a time $t \approx 127$ fs, where the topological charge suddenly jumps to $Q = -1$.

As discussed in refs. [52–54] and illustrated in Fig. 2b, skyrmions in lattice systems experience no real topological stability and are in practice only protected by an energy barrier. By looking at the energy per spin $\epsilon = E/N$ (Fig. 1c), we note that it takes the system about 100 fs to transfer energy from the itinerant s-electrons to the d-electron spins and overcome the barrier. Therefore, the excitation of the d-electron spin system is delayed with respect to the s-electron system, and the skyrmion is created sometime after the pulse has passed.

The demonstration of photo-induced skyrmion nucleation on ultrafast timescales via excitation of the s-electron subsystem constitutes the central result of this work. To pin down the factors contributing to skyrmion photo generation, an explicit description of the s-electron dynamics is necessary. This will become clear as we critically assess the microscopic mechanism behind skyrmion excitation and its parameter dependence. In particular, a

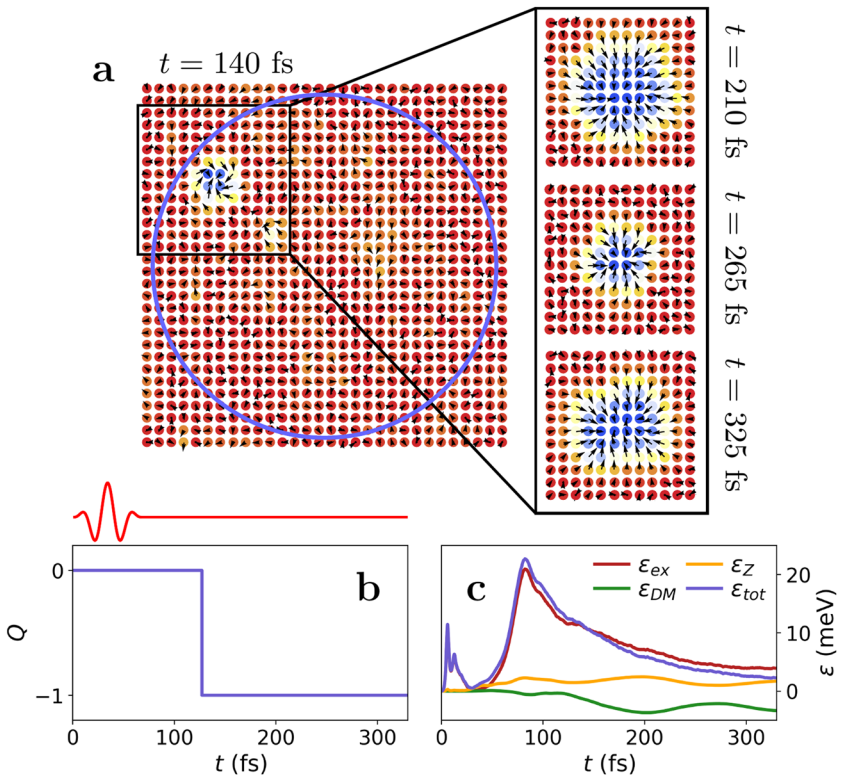

Fig. 1 Laser-induced skyrmion nucleation. a Spin textures of the *d*-electron system at $t = 140$ fs (just after skyrmion excitation), 210, 265, and 325 fs. The coloring shows the out-of-plane component of the spin vector ranging from $S_z = -1$ (blue) to $S_z = 1$ (red). The system has 30×30 sites and the spin parameters are $J = 50$, $D = 25$, and $B = 10$ meV. The *s*-electrons parameters are $t = 1$ and $a = 0.5$ eV, and the *s*–*d* exchange coupling is $g = 2.5$ eV. The laser has a field strength $E = 10^9$ V/m, frequency $\hbar\omega = 0.5$ eV, pulse length $\tau = 30$ fs, and a spot size of ≈14 nm (indicated by the blue circle). The time-dependent electric field is schematically shown above panel (**b**). **b**, **c** Topological charge Q and the energy per spin $\epsilon = E/N$ as a function of time. The total energy $\epsilon_{\rm tot}$ is decomposed into the exchange, DM and Zeeman contributions ϵ_{ex}, ϵ_{DM}, and ϵ_Z.

microscopic analysis of the skyrmion photo-excitation process reveals the *s*–*d* exchange and the spin-orbit interaction among the *s*-electrons as the key parameters determining the skyrmion excitation probability. This identification allows the skyrmion excitation probability to be optimized through material engineering, by manipulating these parameters by material choices, optical drives and interlayer twisting.

Energetics of skyrmion formation

Starting with the equilibrium properties of the *d*-electron spin system, Fig. 2a shows the magnetic state as a function of external magnetic field B and DMI D. The equilibrium state is found by simulated annealing to a target temperature $k_BT/J = 0.02$ using the Monte Carlo Metropolis algorithm[33], corresponding to $T = 11.5$ K for $J = 50$ meV. To minimize stochastic effects in the phase diagram and the subsequent dynamics, the final state for each set of parameters is averaged over 100 Monte Carlo realizations. We find three competing equilibrium phases: a spin spiral phase, a FM phase, and a skyrmion crystal (SkX) phase. To excite skyrmions from an initially FM state, we choose the spin parameters $D/J = 0.5$ and $B/J = 0.2$ close to the FM-SkX phase boundary, as indicated by the orange dot in Fig. 2a. This is in good agreement with the parameters of CoFeB/Ta.

To understand how the *s*-electrons influence the magnetic state, we calculate the excitation energy of a single skyrmion on top of the FM state, $E = E_{Sk} - E_{FM}$, as a function of skyrmion radius R and *s*–*d* exchange g (Fig. 2b). Here, E_{Sk} is the energy of the coupled system for the spin configuration, $\mathbf{n}(\mathbf{r}) = (-xf(u), -yf(u), 1 - 2e^{-u^2})$, where $f(u) = (2/Ru)(e^{-u^2} - e^{-2u^2})^{1/2}$, $u = r/R$ and r is measured from the center of the system. We have verified that this skyrmion profile agrees very well with numerical results for a relaxed skyrmion (see Supplementary Note 5). As shown in Fig. 2b, there is for the pure spin system ($g = 0$) an energy barrier of $E \approx 0.75$ eV to overcome to excite a skyrmion of finite radius, while for $g = 2.5$ the barrier is reduced to $E \approx 0.15$ eV. In addition, for $g \gtrsim 2$, the skyrmion state is lower in energy than the FM state. Due to the reduction of the energy barrier with increasing g, a lower laser fluence is expected to be required to excite skyrmions at the larger coupling.

The role of spin–orbit interactions

Since a strong *s*–*d* exchange is expected to facilitate skyrmion photo-excitation, we here explore this limit further. Additional insight into the microscopic mechanism behind the excitation process can be gained by deriving an effective equation of motion for the *d*-electron spins in this limit. For large g, *s*-electrons with spin antiparallel to the localized *d*-electron moments will be penalized by an energy ~$2g$, and for $g \to \infty$ the antiparallel component vanishes[55].

To exploit this fact we adopt a continuum description and perform a local gauge transformation to align the *s*-electron spins with the localized *d*-electron moments (see Supplementary Note 6). Eliminating the antiparallel spin component to the lowest order gives a modified Landau–Lifshitz equation

$$\partial_t \mathbf{n} = -\frac{a^2}{\hbar M}\left(\mathbf{n} \times [\mathbf{B}_s + \frac{1}{2}\boldsymbol{\alpha}_s \times \mathbf{j}_e] + \hbar(\mathbf{j}_s \cdot \nabla)\mathbf{n}\right). \quad (3)$$

The prefactor describes the total magnetization density $M = S + ms$, where m is the local *s*-electron spin density and $s = 1/2$, that appears since for $g \to \infty$ the *s*- and *d*-electron spins form an effective magnetic moment of magnitude M. The effective magnetic field $\mathbf{B}_s$

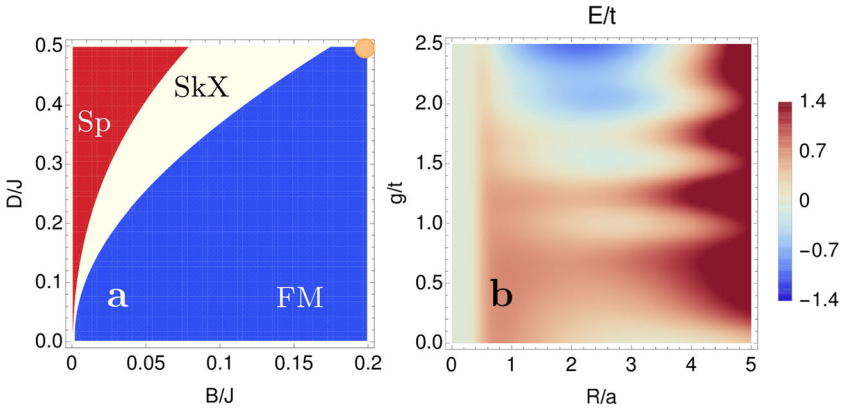

Fig. 2 Equilibrium magnetic properties. a Magnetic phase diagram of the isolated *d*-electron spin system ($g = 0$) as a function of external magnetic field B and Dzyaloshinskii–Moriya interaction (DMI) D. Blue areas indicate a ferromagnetic (FM) state, red areas a spiral (Sp) state and white areas a skyrmion crystal (SkX) state. **b** Excitation energy $E = E_{Sk} - E_{FM}$ of a single skyrmion as a function of skyrmion radius R and s–d exchange g, for the parameters $J = 50$, $D = 25$, and $B = 10$ meV, $t_s = 1$ and $\alpha_s = 0.5$ eV. The orange dot in (**a**) indicates the values of the *d*-electron spin parameters used in (**b**).

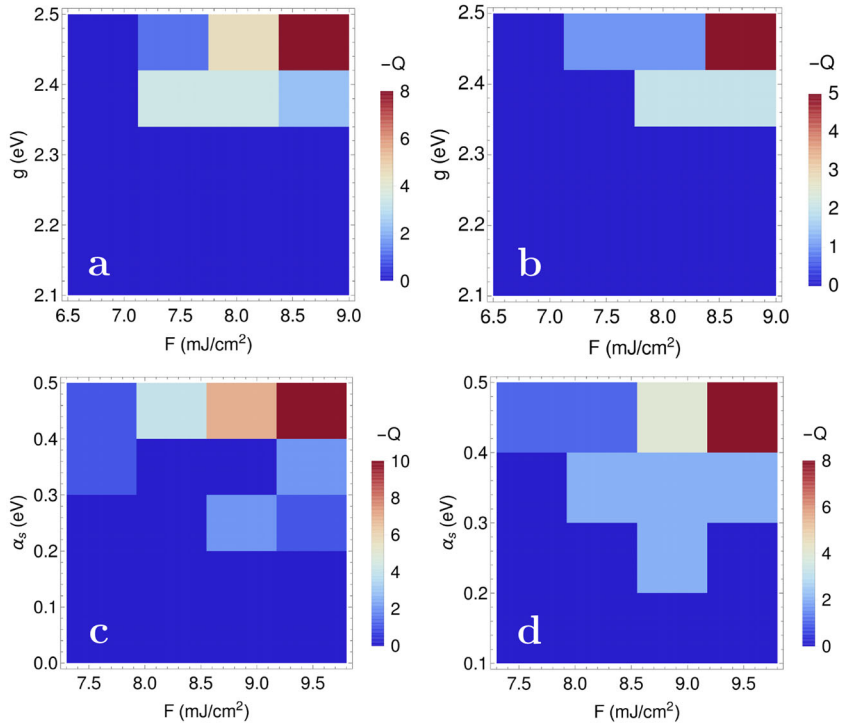

Fig. 3 Parameter dependence of skyrmion excitation. a, **b** Topological charge Q at $t \approx 320$ fs as a function of laser fluence F and spin–electron coupling g, for a spin–orbit coupling $\alpha_s = 0.5$ eV. **c**, **d** Topological charge Q at $t \approx 320$ fs as a function of laser fluence F and spin–orbit coupling α_s, for a spin–electron coupling $g = 2.5$ eV. Panels **a** and **c** show the topological charge for a magnetic field $B = 7.5$ meV, and panels **b** and **d** for $B = 10$ meV. The system is square lattice with 30×30 sites with *d*-electron spin parameters $J = 50$ and $D = 25$ meV, and *s*-electron hopping $t_s = 1$ eV. The laser has a photon energy $\hbar\omega = 0.5$ eV, pulse duration $\tau = 30$ fs, and spot size ≈ 14 nm.

is determined by the interactions $J \to J + \rho t_s/2$ and $D \to D + \rho\alpha_s/2$ that are renormalized by the interaction with the *s*-electrons, where ρ is the density of *s*-electrons with spins parallel to the *d*-electron magnetic moments. The term proportional to the *s*-electron charge current $\mathbf{j}_e$ describes a spin-orbit induced effective magnetic field, which for a Rashba interaction lies in the substrate plane, and the last term describes a coupling to the *s*-electron spin current $\mathbf{j}_s$.

For a FM system with $\mathbf{n}(\mathbf{r}) = \mathbf{n}$, $\partial_i \mathbf{n} = 0$ and the last term of Eq. (3) vanishes. The dominant coupling between the *s*-electrons and the *d*-electron magnetic moments is then given by the term proportional to $\mathbf{j}_e$. For a current $\mathbf{j}_e = j_e \hat{\mathbf{e}}_x$ (as induced by a linearly polarized laser) this term generates an in-plane magnetic field $\mathbf{B}_{so}(\mathbf{r}, t) = \alpha_s j_e \hat{\mathbf{e}}_y$ tilting the spins away from the *z*-axis. For zero spin–orbit coupling $\alpha_s = 0$, the only effect of the *s*-electrons is to renormalize the exchange parameter. Thus, without *s*-electron spin-orbit coupling, skyrmion excitation will be strongly suppressed. This has been confirmed in all our simulations, where we always found no excited skyrmions for $\alpha_s = 0$ within the parameter range considered.

Parameter dependence of skyrmion excitation

In Fig. 3a, b, we show the topological charge Q as a function of laser fluence F and s–d exchange g. For values of g below ≈ 2.3 no

skyrmions are excited, while for larger values of g we find the topological charge to be an increasing function of F, with an approximately linear dependence (the spin configurations containing multiple skyrmions are shown in Supplementary Note 7). This is in agreement with the expectation from Fig. 2b: a finite amount of energy, which decreases with g, must be supplied in order to overcome the skyrmion excitation barrier. The results also qualitatively agree with the trend found in recent experiments[52]. In Fig. 3c, d, we show the topological charge Q as a function of fluence F and s-electron spin–orbit coupling α_s. As expected from the discussion of the strong-coupling limit above, a finite value of α_s is needed for skyrmion nucleation to occur. Our results indicate the needed value of α_s depends on the fluence of the laser as well as the remaining parameters. We have also explored the polarization dependence of the skyrmion excitation process, and find no qualitative differences between linear and circularly polarized pulses. Again, this is in agreement with the experimental findings of ref. [52].

Material realizations

As shown above, favorable conditions to photo-induced skyrmions are a non-zero s-electron spin–orbit interaction and a large s–d exchange. Since the equilibrium state of the system can be controlled by external magnetic and electric fields (the Rashba-induced DMIs at an interface can be manipulated via a perpendicular electric field), we assume the equilibrium system is close to the FM-SkX phase boundary. These conditions are likely to be satisfied in transition metal monolayers and thin films[56], where the s–d exchange is naturally strong and spin–orbit interactions are enhanced by interfacial inversion symmetry breaking. This includes in particular the well-studied systems Fe/Ir(111) and Pd/Fe/Ir(111)[13,43,57]. Another interesting class of systems is twisted magnetic van der Waals bilayers, which have strong spin–orbit interactions and whose local interactions can be tuned via the twist angle[28,58].

DISCUSSION

We have proposed a microscopic theory of laser-induced skyrmion excitation based on a two-band electronic model. Numerical simulations predict ultrafast skyrmion excitation in the limit of strong s–d exchange, which we attribute to the effective magnetic field generated by spin–orbit interactions and charge currents among the itinerant s-electrons. Our results show that an explicit treatment of itinerant s-electrons and their dynamic interaction with the localized d-electron spins is an essential ingredient in understanding skyrmion photo-excitation.

The proposed theory predicts photo-excitation of skyrmions on a 100 fs second timescale and opens up for ultrafast manipulation of topological magnetic textures. In addition, both the s–d exchange and interfacial Rashba interaction are in principle controllable via material choices and external fields, leading to large possibilities of engineering candidate materials such as transition metal thin films and van der Waals bilayers to optimize the skyrmion excitation. Our theory can also be applied to study the influence of itinerant electrons on skyrmion transport[33], magnon and electron excitations in SkXs[59–61], and charged skyrmions on topological insulator surfaces[62], thus opening an avenue to explore a vast range of physical phenomena in non-equilibrium magnetic systems.

METHODS

Coupled equations of motion

Using the Heisenberg equation of motion for the d-electron spin operators, and defining $\mathbf{n}_i = \mathbf{S}_i/S$ (with $S = |\mathbf{S}_i|$), the spin dynamics is governed by the Landau–Lifshitz equation[63,64]

$$\frac{\partial \mathbf{n}_i}{\partial t} = \mathbf{n}_i \times \left(\sum_{\langle j \rangle} S\left[J_{ij}\mathbf{n}_j + \mathbf{D}_{ij} \times \mathbf{n}_j \right] + \mathbf{B} + g\langle \hat{\mathbf{s}}_i \rangle \right), \tag{4}$$

where the last term couples the classical d-electron spins to the quantum averages of the s-electron spins. The quantum dynamics of the itinerant s-electrons and their coupling to the classical d-electron spins are described via the electronic single-particle density matrix $\rho_{ij}(t)$, governed by the equation of motion

$$\frac{d}{dt}\rho_{ij}(t) + i[H_s(t) + H_{s-d}(\mathbf{n}(t)), \rho(t)]_{ij} = 0. \tag{5}$$

Here i and j are combined spin and orbital indexes, $i = n\sigma$, with n a site and σ a spin-label. Knowledge of ρ_{ij} allows obtaining any single-particle expectation value of the s-electrons, such as the spins $\mathbf{s}_i = \mathrm{Tr}_{\sigma\sigma'}(\boldsymbol{\tau}\rho_{ij})$ and spin densities $n_{sn\sigma} = \rho^{\sigma\sigma}_{nn}$, by selecting the appropriate components of ρ_{ij}. The equation of motion for the density matrix can be derived from the general theory of non-equilibrium Green's functions[33,65], and allows for straightforward inclusion of electronic reservoirs and interactions among the s-electrons. However, since this significantly increases the computational effort, we here for simplicity take our system to be isolated and consider non-interacting s-electrons.

Definition of the topological charge

To quantify the topology of the classical spin texture we use the lattice topological charge Q defined by[66]

$$Q = \frac{1}{4\pi}\sum_{\Delta} \Omega_{\Delta}. \tag{6}$$

In this definition the lattice is triangulated and Ω_Δ corresponds to the signed area of the spherical triangle spanned by three neighboring spins, given by[66]

$$\begin{aligned} e^{i\Omega_\Delta/2} &= \tfrac{1}{\rho}\left(1 + \mathbf{S}_i\cdot\mathbf{S}_j + \mathbf{S}_j\cdot\mathbf{S}_k + \mathbf{S}_k\cdot\mathbf{S}_i + i\eta_{ijk}\mathbf{S}_i\cdot[\mathbf{S}_j\times\mathbf{S}_k]\right) \\ \rho &= \sqrt{2(1+\mathbf{S}_i\cdot\mathbf{S}_j)(1+\mathbf{S}_j\cdot\mathbf{S}_k)(1+\mathbf{S}_k\cdot\mathbf{S}_i)}, \end{aligned} \tag{7}$$

where $\eta_{ijk} = +1(-1)$ if the path $i \to j \to k \to i$ is positively (negatively) oriented. The surface area Ω_Δ is well-defined everywhere except at the zero-measure set $\mathbf{S}_i\cdot(\mathbf{S}_j\times\mathbf{S}_k) = 0$ and $1 + \mathbf{S}_i\cdot\mathbf{S}_j + \mathbf{S}_j\cdot\mathbf{S}_k + \mathbf{S}_k\cdot\mathbf{S}_i < 0$, where $e^{i\Omega_\Delta/2}$ has a branch cut. The topological charge is a compact, convenient indicator of the presence of a non-trivial spin texture: For a single skyrmion $Q = -1$, for a single antiskyrmion $Q = 1$, and for a cluster of skyrmions and antiskyrmions $Q = \sum_i Q_i$ with Q_i their individual charges.

DATA AVAILABILITY

All the data supporting the findings of this study are available from the corresponding authors upon reasonable request.

CODE AVAILABILITY

The codes used to generate the data of this study are available from the corresponding authors upon reasonable request.

Received: 7 June 2021; Accepted: 24 February 2022;
Published online: 08 April 2022

REFERENCES

1. Bogdanov, A. N. & Rößler, U. K. Chiral symmetry breaking in magnetic thin films and multilayers. *Phys. Rev. Lett.* **87**, 037203 (2001).
2. Rößler, U. K., Bogdanov, A. N. & Pfleiderer, C. Spontaneous skyrmion ground states in magnetic metals. *Nature* **442**, 797–801 (2006).
3. Muhlbauer, S. et al. Skyrmion lattice in a chiral magnet. *Science* **323**, 915–919 (2009).
4. Yu, X. Z. et al. Real-space observation of a two-dimensional skyrmion crystal. *Nature* **465**, 901–904 (2010).
5. Yang, G., Stano, P., Klinovaja, J. & Loss, D. Majorana bound states in magnetic skyrmions. *Phys. Rev. B* **93**, 224505 (2016).
6. Chisnell, R. et al. Topological magnon bands in a kagome lattice ferromagnet. *Phys. Rev. Lett.* **115**, 147201 (2015).

7. Cheng, R., Okamoto, S. & Xiao, D. Spin nernst effect of magnons in collinear antiferromagnets. *Phys. Rev. Lett.* **117**, 217202 (2016).
8. Nakata, K., Klinovaja, J. & Loss, D. Magnonic quantum hall effect and wiedemann-franz law. *Phys. Rev. B* **95**, 125429 (2017).
9. Nakata, K., Kim, S. K., Klinovaja, J. & Loss, D. Magnonic topological insulators in antiferromagnets. *Phys. Rev. B* **96**, 224414 (2017).
10. Kasahara, Y. et al. Majorana quantization and half-integer thermal quantum hall effect in a kitaev spin liquid. *Nature* **559**, 227–231 (2018).
11. Sampaio, J., Cros, V., Rohart, S., Thiaville, A. & Fert, A. Nucleation, stability and current-induced motion of isolated magnetic skyrmions in nanostructures. *Nat. Nanotechnol.* **8**, 839–844 (2013).
12. Nagaosa, N. & Tokura, Y. Topological properties and dynamics of magnetic skyrmions. *Nat. Nanotechnol.* **8**, 899–911 (2013).
13. Romming, N., Kubetzka, A., Hanneken, C., von Bergmann, K. & Wiesendanger, R. Field-dependent size and shape of single magnetic skyrmions. *Phys. Rev. Lett.* **114**, 177203 (2015).
14. Chauwin, M. et al. Skyrmion logic system for large-scale reversible computation. *Phys. Rev. Appl.* **12**, 064053 (2019).
15. Rex, S., Gornyi, I. V. & Mirlin, A. D. Majorana bound states in magnetic skyrmions imposed onto a superconductor. *Phys. Rev. B* **100**, 064504 (2019).
16. Finazzi, M. et al. Laser-induced magnetic nanostructures with tunable topological properties. *Phys. Rev. Lett.* **110**, 177205 (2013).
17. Ogawa, N., Seki, S. & Tokura, Y. Ultrafast optical excitation of magnetic skyrmions. *Sci. Rep.* **5**, 9552 (2015).
18. Je, S.-G. et al. Creation of magnetic skyrmion bubble lattices by ultrafast laser in ultrathin films. *Nano Lett.* **18**, 7362–7371 (2018).
19. Fujita, H. & Sato, M. Ultrafast generation of skyrmionic defects with vortex beams: printing laser profiles on magnets. *Phys. Rev. B* **95**, 054421 (2017).
20. Berruto, G. et al. Laser-induced skyrmion writing and erasing in an ultrafast cryo-lorentz transmission electron microscope. *Phys. Rev. Lett.* **120**, 117201 (2018).
21. Khoshlahni, R., Qaiumzadeh, A., Bergman, A. & Brataas, A. Ultrafast generation and dynamics of isolated skyrmions in antiferromagnetic insulators. *Phys. Rev. B* **99**, 054423 (2019).
22. Polyakov, O. P., Gonoskov, I. A., Stepanyuk, V. S. & Gross, E. K. U. Generation of magnetic skyrmions by focused vortex laser pulses. *J. Appl. Phys.* **127**, 073904 (2020).
23. Tong, Q., Liu, F., Xiao, J. & Yao, W. Skyrmions in the moiré of van der waals 2d magnets. *Nano Lett.* **18**, 7194–7199 (2018).
24. McIver, J. W. et al. Light-induced anomalous hall effect in graphene. *Nat. Phys.* **16**, 38–41 (2019).
25. Sato, S. A. et al. Microscopic theory for the light-induced anomalous hall effect in graphene. *Phys. Rev. B* **99**, 214302 (2019).
26. Kerelsky, A. et al. Maximized electron interactions at the magic angle in twisted bilayer graphene. *Nature* **572**, 95–100 (2019).
27. Wang, L. et al. Correlated electronic phases in twisted bilayer transition metal dichalcogenides. *Nat. Mater.* **19**, 861–866 (2020).
28. Sivadas, N., Okamoto, S., Xu, X., Fennie, C. J. & Xiao, D. Stacking-dependent magnetism in bilayer Crl3. *Nano Lett.* **18**, 7658–7664 (2018).
29. Kennes, D. M. et al. Moiré heterostructures as a condensed-matter quantum simulator. *Nat. Phys.* **17**, 155–163 (2021).
30. Mentink, J. H., Balzer, K. & Eckstein, M. Ultrafast and reversible control of the exchange interaction in mott insulators. *Nat. Commun.* **6**, 6708 (2015).
31. Stepanov, E. A., Dutreix, C. & Katsnelson, M. I. Dynamical and reversible control of topological spin textures. *Phys. Rev. Lett.* **118**, 157201 (2017).
32. Claassen, M., Jiang, H.-C., Moritz, B. & Devereaux, T. P. Dynamical time-reversal symmetry breaking and photo-induced chiral spin liquids in frustrated mott insulators. *Nat. Commun.* **8**, 1192 (2017).
33. Boström, E. V. & Verdozzi, C. Steering magnetic skyrmions with currents: a nonequilibrium green's functions approach. *Phys. Status Solidi B* **256**, 1800590 (2019).
34. Viñas Boström, E. et al. Light-induced topological magnons in two-dimensional van der Waals magnets. *Sci. Post Phys.* **9**, 61 (2020).
35. Bajpai, U. & Nikolić, B. K. Spintronics meets nonadiabatic molecular dynamics: geometric spin torque and damping on dynamical classical magnetic texture due to an electronic open quantum system. *Phys. Rev. Lett.* **125**, 187202 (2020).
36. Ghosh, S., Freimuth, F., Gomonay, O., Blügel, S. & Mokrousov, Y. Driving spin chirality by electron dynamics in laser-excited antiferromagnets. Preprint at *arXiv* https://arxiv.org/abs/2011.01670 (2020).
37. Schrieffer, J. R. & Wolff, P. A. Relation between the anderson and kondo hamiltonians. *Phys. Rev.* **149**, 491–492 (1966).
38. Sentef, M. A., Li, J., Künzel, F. & Eckstein, M. Quantum to classical crossover of floquet engineering in correlated quantum systems. *Phys. Rev. Res.* **2**, 033033 (2020).
39. Dzyaloshinsky, I. A thermodynamic theory of "weak" ferromagnetism of antiferromagnetics. *J. Phys. Chem. Solids* **4**, 241 (1958).
40. Moriya, T. Anisotropic superexchange interaction and weak ferromagnetism. *Phys. Rev.* **120**, 91 (1960).
41. Lieb, E. H. The classical limit of quantum spin systems. *Commun. Math. Phys.* **31**, 327–340 (1973).
42. Fradkin, E. *Field Theories of Condensed Matter Physics* (Cambridge University Press, 2013).
43. Heinze, S. et al. Spontaneous atomic-scale magnetic skyrmion lattice in two dimensions. *Nat. Phys.* **7**, 713–718 (2011).
44. Brown, W. F. Thermal fluctuations of a single-domain particle. *Phys. Rev.* **130**, 1677–1686 (1963).
45. Brächer, T. et al. Detection of short-waved spin waves in individual microscopic spin-wave waveguides using the inverse spin hall effect. *Nano Lett.* **17**, 7234–7241 (2017).
46. Qin, Z. et al. Stabilization and reversal of skyrmion lattice in Ta/CoFeB/MgO multilayers. *ACS Appl. Mater. Interfaces* **10**, 36556–36563 (2018).
47. Casiraghi, A. et al. Individual skyrmion manipulation by local magnetic field gradients. *Commun. Phys* **2**, 145 (2019).
48. Zener, C. Interaction between the *d*-shells in the transition metals. ii. ferromagnetic compounds of manganese with perovskite structure. *Phys. Rev.* **82**, 403–405 (1951).
49. Anderson, P. W. & Hasegawa, H. Considerations on double exchange. *Phys. Rev.* **100**, 675–681 (1955).
50. Onose, Y., Okamura, Y., Seki, S., Ishiwata, S. & Tokura, Y. Observation of magnetic excitations of skyrmion crystal in a helimagnetic insulator Cu_2OSeO_3. *Phys. Rev. Lett.* **109**, 037603 (2012).
51. Mochizuki, M. Spin-wave modes and their intense excitation effects in skyrmion crystals. *Phys. Rev. Lett.* **108**, 017601 (2012).
52. Je, S.-G. et al. Direct demonstration of topological stability of magnetic skyrmions via topology manipulation. *ACS Nano* **14**, 3251–3258 (2020).
53. Cortés-Ortuño, D. et al. Thermal stability and topological protection of skyrmions in nanotracks. *Sci. Rep.* **7**, 4060 (2017).
54. von Malottki, S., Bessarab, P. F., Haldar, S., Delin, A. & Heinze, S. Skyrmion lifetime in ultrathin films. *Phys. Rev. B* **99**, 060409(R) (2019).
55. Volovik, G. E. Linear momentum in ferromagnets. *J. Phys. C* **20**, L83–L87 (1987).
56. Fert, A., Reyren, N. & Cros, V. Magnetic skyrmions: advances in physics and potential applications. *Nat. Rev. Mater.* **2**, 17031 (2017).
57. von Bergmann, K., Menzel, M., Kubetzka, A. & Wiesendanger, R. Influence of the local atom configuration on a hexagonal skyrmion lattice. *Nano Lett.* **15**, 3280–3285 (2015).
58. Tong, Q. et al. Topological mosaics in moiré superlattices of van der Waals heterobilayers. *Nat. Phys.* **13**, 356–362 (2016).
59. Díaz, S. A., Hirosawa, T., Loss, D. & Psaroudaki, C. Spin wave radiation by a topological charge dipole. *Nano Lett.* **20**, 6556–6562 (2020).
60. Hamamoto, K., Ezawa, M. & Nagaosa, N. Quantized topological hall effect in skyrmion crystal. *Phys. Rev. B* **92**, 115417 (2015).
61. Lado, J. L. & Fernández-Rossier, J. Quantum anomalous Hall effect in graphene coupled to skyrmions. *Phys. Rev. B* **92**, 115433 (2015).
62. Nomura, K. & Nagaosa, N. Electric charging of magnetic textures on the surface of a topological insulator. *Phys. Rev. B* **82**, 161401(R) (2010).
63. Lakshmanan, M. The fascinating world of the Landau–Lifshitz–Gilbert equation: an overview. *Philos. Trans. R. Soc. A* **369**, 1280–1300 (2011).
64. Baryakhtar, V. G. & Ivanov, B. A. The Landau-Lifshitz equation: 80 years of history, advances, and prospects. *Low Temp. Phys.* **41**, 663–669 (2015).
65. Petrović, M. D., Popescu, B. S., Bajpai, U., Plecháč, P. & Nikolić, B. K. Spin and charge pumping by a steady or pulse-current-driven magnetic domain wall: a self-consistent multiscale time-dependent quantum-classical hybrid approach. *Phys. Rev. Appl.* **10**, 054038 (2018).
66. Berg, B. & Lüscher, M. Definition and statistical distributions of a topological number in the lattice $o(3)\sigma$-model. *Nucl. Phys. B* **190**, 412–424 (1981).

ACKNOWLEDGEMENTS

E.V.B acknowledges stimulating discussions with Florian Eich during the early stages of this work. We acknowledge support by the Max Planck Institute New York City Center for Non-Equilibrium Quantum Phenomena and by the Swedish Research Council. We also acknowledge support from the European Research Council (ERC-2015-AdG694097), the Cluster of Excellence "Advanced Imaging of Matter" (AIM), and Grupos Consolidados (IT1249-19). The Flatiron Institute is a Division of the Simons Foundation.

AUTHOR CONTRIBUTIONS

E.V.B. performed the analytical and numerical calculations, with input from and under the supervision of A.R and C.V. The project was conceived by E.V.B and C.V, and all authors collaborated in writing the paper.

FUNDING

Open Access funding enabled and organized by Projekt DEAL.

COMPETING INTERESTS

The authors declare no competing interests.

ADDITIONAL INFORMATION

Supplementary information The online version contains supplementary material available at https://doi.org/10.1038/s41524-022-00735-5.

Correspondence and requests for materials should be addressed to Emil Viñas Boström, Angel Rubio or Claudio Verdozzi.